Petroleum Science 19 (2022) 459–471

Contents lists available at ScienceDirect

Petroleum Science

journal homepage: www.keaipublishing.com/en/journals/petroleum-science

Original Paper

Pore structure evolution of lacustrine organic-rich shale from the second member of the Kongdian formation in the Cangdong Sag, Bohai Bay Basin, China

Xiao-Ping Liu [a, b, *], Ming Guan [a, b, c], Zhi-Jun Jin [d, e], Zhe Cao [e, f], Jin Lai [a, b], Lun-Ju Zheng [g], Wen-Qi Li [a, b], Biao Sun [a, b], Shan-Yong Chen [h]

[a] State Key Laboratory of Petroleum Resources and Prospecting, China University of Petroleum (Beijing), Beijing, 102249, China
[b] College of Geosciences, China University of Petroleum (Beijing), Beijing, 102249, China
[c] Research Institute of Petroleum Exploration and Development, China National Petroleum Corporation, Beijing, 100083, China
[d] Institute of Energy, Peking University, Beijing, 100871, China
[e] State Key Laboratory of Shale Oil and Gas Enrichment Mechanisms and Effective Development, Beijing, 100083, China
[f] Sinopec Petroleum Exploration and Production Research Institute, Beijing, 102206, China
[g] Wuxi Petroleum Geology Institute, Research Institute of Petroleum Exploration and Development, Sinopec, Wuxi, Jiangsu 214126, China
[h] PetroChina Dagang Oil Field Company, Tianjin, 300280, China

ARTICLE INFO

Article history:
Received 12 January 2021
Accepted 13 August 2021
Available online 8 December 2021

Edited by Jie Hao

Keywords:
Lacustrine shale
Pyrolysis
Thermal maturity
Pore structure evolution
Hydrocarbon generation evolution

ABSTRACT

Pyrolysis experiments were conducted on lacustrine organic-rich shale from Cangdong Sag in Bohai Bay Basin, China, to investigate the impact of hydrocarbon generation on shale pore structure evolution. Thermal evolution is found to control the transformation of organic matter, hydrocarbon products characteristics, and pore structure changes. Furthermore, pore volume and specific surface area increase with increasing maturity. In low-mature stage, the retained oil content begins to increase, pore volumes show slight changes, and primary pores are occluded by the generated crude oil of high molecular weight and density. In the oil-window stage, the retained oil content rapidly increases and reaches maximum, and pore volumes gradually increase with increasing thermal maturity. At high mature stage, the retained oil content begins to decrease, and the pore volume increases considerably owing to the expulsion of liquid hydrocarbon. In over mature stage, natural gas content significantly increases and kerogen transforms to asphalt. Numerous organic pores are formed and the pore size gradually increases, resulting from the connection of organic pores caused the increasing thermal stress. This study lays a foundation for understanding variation of hydrocarbon products during the thermal evolution of lacustrine shales and its relationship with the evolution of shale reservoirs.

1. Introduction

Shale is defined as a sedimentary rock that is layered and fine-grained (>50% of particles, grain size <62.5 μm) (Milliken, 2014; Lazar et al., 2015); thus, it is nearly interchangeable with the term “mudrock” (Merriman et al., 2003; Ilgen et al., 2017; Liu et al., 2020). Shale usually contains abundant organic matter sourced from algae (e.g., planktonic algae and phytoplankton), bacteria, or vascular land plants. Furthermore, shale generally exhibits immense capillary pressure (Hutton, 1987; Schlömer and Krooss, 1997), acting as a source rock or a cap rock (Hunt, 1996; Aplin and Macquaker, 2011). Commercial production from shale reservoirs around the world has justified their prospects as effective unconventional hydrocarbon reservoirs (Jarvie, 2012a, 2012b; Yang et al., 2019; Zou et al., 2019; Nie et al., 2020; Solarin et al., 2020).

Various types of pores, including interparticle and intraparticle pores as well as organic pores, constitute the main storage space for shale oil and gas, with pore sizes as small as nanoscale (Loucks et al., 2009, 2012; Slatt and O'Brien, 2011; Ougier-Simonin et al., 2016). Considering the complex pore systems in shale, various techniques have been developed to evaluate shale pore structure

* Corresponding author. State Key Laboratory of Petroleum Resources and Prospecting, China University of Petroleum (Beijing), Beijing, 102249, China.
E-mail address: liuxiaoping@cup.edu.cn (X.-P. Liu).

https://doi.org/10.1016/j.petsci.2021.12.010

(Chalmers et al., 2009; Loucks et al. 2009, 2012; Ougier-Simonin et al., 2016; Lai et al., 2018). Visualization methods, including scanning electron microscopy (Chalmers et al., 2012), transmission electron microscopy (Wirth, 2009), focused ion beam–scanning electron microscopy (Goral et al., 2019), and nano-computed tomography (Sun et al., 2018), are used to examine the geometric morphology and connectivity of shale pores. Pore characteristics are quantified by other techniques, including gas adsorption (Wei et al., 2016), helium pycnometry (Yang et al., 2010), mercury injection (Kuila and Prasad, 2013), small-angle/ultrasmall-angle neutron scattering (Clarkson et al., 2013), and nuclear magnetic resonance (Xu et al., 2015).

Pore evolution during the burial process or during thermal maturation is an important aspect for predicting the occurrence of effective reservoirs (Athy, 1930; Selley, 1978; McBride, 1989; Chandra et al., 2021). In the case of conventional reservoirs, pore structure evolution is mainly affected by diagenesis (Selley, 1978; Land et al., 1987; Teillet et al., 2019). The pore structure evolution of a shale reservoir can be attributed to the coupling of diagenesis and hydrocarbon generation (Aplin and Macquaker, 2011; Milliken and Curtis, 2016; Milliken et al., 2019), as influenced by mineral transformation (Deng et al., 2021), hydrocarbon generation and migration (Tang et al., 2015a), expansion and shrinkage of kerogen (Alcantar-Lopez, 2016), overpressure (Li et al., 2019), and organic–inorganic interactions (Seewald, 2003), among other factors. Hydrocarbon generation, which is primarily a function of thermal maturation, plays an important role in the development and evolution of pores in shales (Camp, 2014; Han et al., 2017; Tang et al., 2015b; Kartz and Arango, 2018). Previous studies have provided insights into the impact of thermal maturation on pore structure changes (Mastalerz et al., 2013; Chen and Xiao, 2014; Tang et al., 2015a; Zargari et al., 2015; Ko et al., 2016; Wu et al., 2019).

However, shale pore evolution remains a matter of little consensus because of among-shale inconsistencies in the relationship between pore changes and thermal maturity. Modica and Lapierre (2012) suggested that pore evolution in shales is governed mainly by kerogen transformation, with a likely limited contribution from mineral matrix pores. Ko et al. (2017) considered depositional and diagenetic processes as important factors governing pore changes in lacustrine mudstones of the Yanchang Formation. The formation of organic pores is known to be closely associated with hydrocarbon generation, as confirmed by studies of artificial maturation and natural thermal evolution (Modica and Lapierre, 2012; Kuchinskiy, 2013; Mastalerz et al., 2013; Chen and Xiao, 2014; Wu et al., 2019; Wang et al., 2020). However, it remains very unclear about thermal maturity relevance to the initial presence of organic pores (Reed et al., 2015; Jennings and Antia, 2013; Han et al., 2017). Moreover, there are discrepancies in organic pore abundance and size during thermal maturation (Curtis et al., 2012; Reed et al., 2012; Mastalerz et al., 2013; Zargari et al., 2015; Han et al., 2017). The occlusion of organic pores and mineral-matrix pores by migrated oil or bitumen has been reported in many previous studies (Loucks et al., 2012; Loucks and Reed, 2014; Löhr et al., 2015; Zargari et al., 2015; Kartz and Arango, 2018). Because changes in the abundance, size, and shape of pores are closely related to hydrocarbon generation in shales, the impact of hydrocarbon generation on pore structure evolution during thermal maturation must be investigated further. Other governing factors, including organic richness (Milliken et al., 2013), organic matter types (Cardott et al., 2015; Guo et al., 2020), mineral compositions (Inan et al., 2018), and rock fabric (Liu et al., 2019), are known to locally control pore structure changes in shale. Therefore, isolating these nonthermal maturity factors is essential for a clear discussion of the impact of thermal maturity on pore structure.

In this study, the pyrolysis technique was applied to study lacustrine shale to minimize the influence of nonthermal maturity factors. The experimental products, including retained hydrocarbon from the shale residues and expelled hydrocarbon, were quantified. Furthermore, the pore structures corresponding to various thermal maturities were analyzed to determine the impact of hydrocarbon generation on pore structure evolution during thermal maturation. The results provide important insights regarding two factors of great importance for exploration and efficient development of shale oil plays: pore spaces and reservoir quality assessment.

2. Geological background

The Cangdong Sag, a Cenozoic rifted lacustrine basin, is a secondary structural unit of the Huanghua Depression in Bohai Bay Basin, China. The second member of the Paleogene Kongdian Formation (Ek_2) in Cangdong Sag was deposited in a deep to semi-deep lacustrine environment during the early stages of the Paleogene. The lithology consists of siltstone, sandstone, and argillaceous dolostone, clastic mudstone, oil shale, etc. The Ek_2 shale possesses high organic matter content, predominantly organic matter types I and II_1 with a small amount of types II_2 and III. Vitrinite reflectance (R_o) values range from 0.4% to 1.3%, and the Ek_2 shale generates mainly liquid oil (Zhao et al., 2020). Recent exploration has demonstrated the considerable potential of the Ek_2 shale oil, and industrial oil production exceeds 20 t/d at several local wells, including wells GD6x1 and KN9 (Zhao et al. 2018a, 2018b, 2019, 2020, 2018b).

In this study, organic-rich shale samples were collected from the Ek_2 shale at well G995 (Fig. 1). Pyrolysis experiments were performed on shale samples with high organic matter abundance (total organic carbon, TOC: 7.87 wt%) and low maturity (burial depth: 2913.76 m; R_o: 0.55%).

3. Experimental procedures

3.1. Pyrolysis experiments

Pyrolysis has been an effective technique for understanding pore development mechanisms during thermal maturation (Wu et al., 2019). Time and temperature are two critical factors that impact the thermal maturity of shale, and a given experimental temperature or duration may result in a similar thermal maturity. Therefore, source rocks at various evolution stages can be obtained by controlling the temperature and time, and the characteristics of a given sample at various stages of evolution can be explored.

The experimental boundary conditions of the pyrolysis experiment in this study were determined to realize the dynamic process of hydrocarbon generation and expulsion according to the previously reported formation pressure and temperature characteristics of the Ek_2 shale in the Cangdong Sag (Dong et al., 2015). The experimental temperatures were set to 300, 325, 350, 375, 400, and 500 °C to distinguish the various evolutionary stages of hydrocarbon generation.

Samples were considered to be in the low mature stage when the simulated temperature was less than 325 °C. The mature stage (i.e. the main “oil-window”) corresponds to the temperature range of 325–375 °C; the high mature stage (i.e. the condensate and wet gas phase) corresponds to the temperature range of 375–400 °C; and the high mature to over mature stage (i.e. the dry gas phase) corresponds to the temperature range of 400–500 °C. The experimental hydrostatic pressures were established based on hypothetical burial depths, and the formation and lithostatic pressures

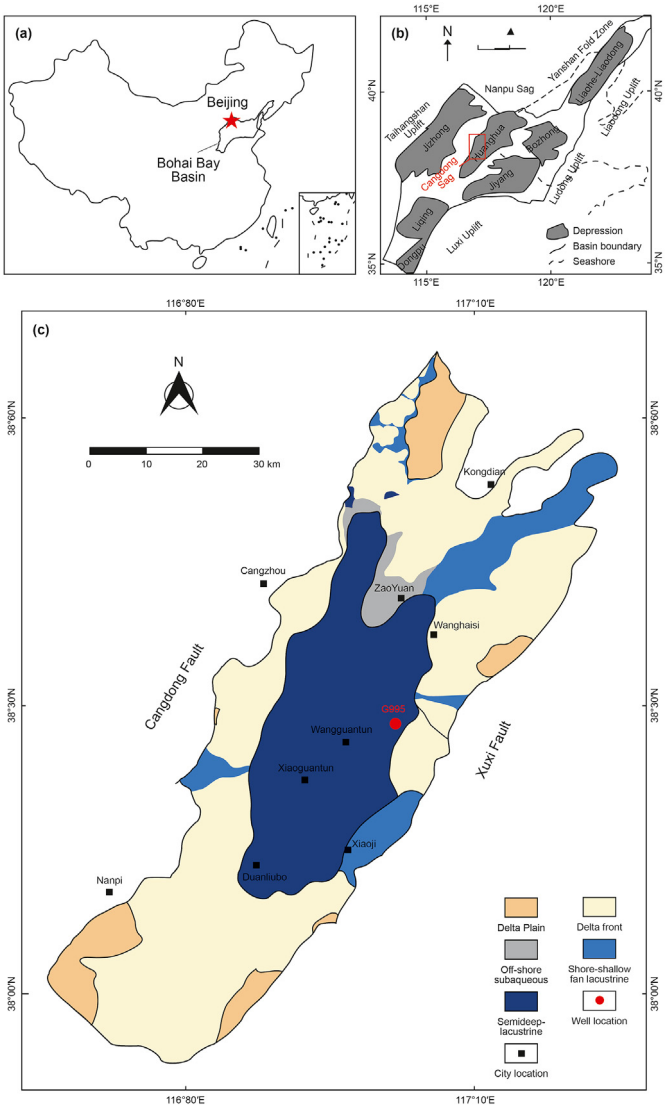

Fig. 1. Location of the study area and sedimentary facies: (a) and (b) location of the Cangdong Sag in Bohai Bay Basin, China, and (c) the sedimentary facies of the Ek_2 and the location of the sampling well (modified from Pu et al. (2016)).

were determined based on the actual pressure conditions of the Ek_2 shale (Dong et al., 2015). The formation pressures, exerted by injecting high-pressure water, were 1.2–1.4 times the hydrostatic pressure. Lithostatic pressures and confining pressures were exerted using oil cylinders. For the pyrolysis experiments, six small core columns (diameter 38 mm, height 50 mm) were obtained from the original core sample.

Pyrolysis experiments were conducted under high-temperature, high-pressure conditions. The heating rate was set at 1 °C/min. After the specified temperature was achieved, that temperature was maintained for 48 h to ensure that the entire system attained a constant temperature. Pore spaces in the pyrolysis experiment were saturated with deionized water, and the overlying static rock pressure and pore fluid pressure were listed in Table 1. A schematic of the experiment is shown in Fig. 2. Hydrocarbon products (expelled hydrocarbons, retained hydrocarbons, and gaseous hydrocarbons) and sample residues were obtained through the pyrolysis experiments.

3.2. Determination of experimental products

The expelled gaseous mixture was analyzed using a 3800 Gas Chromatograph to determine the relative H_2, O_2, N_2, and CO_2 contents as well as gaseous hydrocarbon contents including C_xH_{2x+2}, where $2 \leq x \leq 5$). The volume percentage of each gas component was transformed into an amount in grams according to the ideal gas law (Spigolon et al., 2015). Approximately 50 g of the original sample and solid residues were ground and extracted using the Soxhlet extraction method with dichloromethane (DCM) as the solvent. The residue substance after removal of solvents was considered as the retained hydrocarbon, also known as the extractible organic matter (EOM). The total amount of retained oil was calculated as the product of the total solid residue weight and the weight ratio of the extracted retained hydrocarbon and the extracted residue. In addition to the liquid hydrocarbon collected from the oil collector, some liquid hydrocarbon remained on the autoclave wall and pipe; these were irrigated by dichloromethane after the system was cooled to room temperature, and both were included in measurements of expelled liquid hydrocarbon.

TOC was determined using a LECO CS-200 carbon/sulfur analyzer. Shale powder (approximately 100 mg, 60–80 mesh) was initially digested with dilute hydrochloric acid ($HCl:H_2O$ v/v ratio of 1:9) to eliminate any inorganic carbon. Subsequently, each sample was dried and introduced into the combustion oven to measure TOC. About 50 mg of the powdered sample was used by a Rock-Eval 6 device to determine various pyrolysis parameters, including free hydrocarbon (S_1), thermal cracking hydrocarbon (S_2), peak temperature (T_{max}), and hydrogen index (HI). R_o was measured under an oil-immersed lens through a light microscope equipped with an MSP200 microphotometer as per the SY/T 5124 standard (2012). The nitrogen adsorption test was performed using a JWBK-200C specific surface area and pore-size analyzer. For the mercury pressure test, a Micrometrics Autopore 9520 mercury porosimeter was used; details of the experimental method were described by Guan et al. (2020).

Asphaltenes were precipitated from the obtained extracts and expelled oil using *n*-hexane. Subsequently, the aliphatic, aromatic, and resin fractions were separated using a chromatographic column and various irrigating agents: *n*-hexane, a 2:1 (v/v) mixture of dichloromethane and *n*-hexane, and a 1:1 (v/v) mixture of ethanol and dichloromethane, respectively. The aliphatic components were analyzed using an Agilent 7890 gas chromatograph. The initial temperature was set at 60 °C for 2 min; the sample was then heated at a rate of 10 °C/min up to 160 °C and then at a rate of at 3 °C/min up to 310 °C. The sample was then maintained at 310 °C for 30 min. Helium was used as the carrier gas; the flow rate was 1 mL/min, the ionization energy was 70 eV, and the detection mode was full-scan/multi-ion detection.

4. Results

4.1. Organic geochemistry

The original samples were low mature samples with high abundance of organic matter. Sample maturity increased with increasing temperature. When the temperature was lower than 325 °C ($R_o \leq 0.60\%$), the maturity was low and the TOC decreased slightly. When the temperature was in the range of 325–375 °C ($0.60 < R_o \leq 1.21\%$), the sample entered the mature stage, and the TOC decreased by 52.6% compared with that of the original sample. When the temperature was in the range of 375–400 °C ($1.21\% < R_o \leq 1.42\%$), the sample was in the high mature stage, and

Table 1
Boundary conditions of pyrolysis experiments.

Temperature, °C	Sample	Depth, m	Formation pressure, MPa	Lithostatic pressure, MPa
–	OS	2914	35	71
300	PY-300	2938	35	71
325	PY-325	3209	40	79
350	PY-350	3713	47	94
375	PY-375	4023	53	106
400	PY-400	4231	58	116
500	PY-500	5669	70	141

Note: OS = original sample; sample PY number refers to the simulated temperature of the sample in °C.

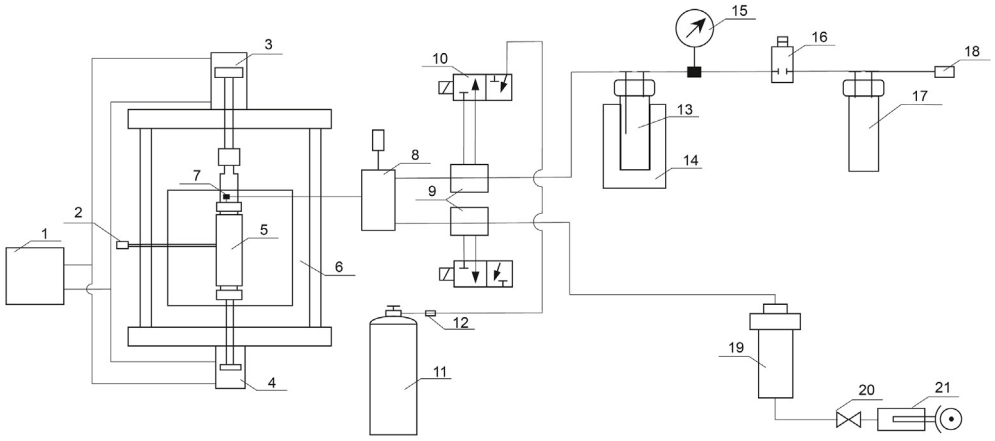

Fig. 2. Schematic of the pyrolysis device: 1. Hydraulic system; 2. Temperature transmitter; 3. Oil cylinder A; 4. Oil cylinder B; 5. Sample cell; 6. Autoclave; 7. Pipe splice; 8. Pressure transmitter; 9. High-pressure pneumatic valve; 10. Two-position, three-way solenoid valves; 11. High-pressure air bottle; 12. Decompression valve; 13. Oil collector; 14. Cold trap; 15. Pressure gage; 16. Magnetic valve; 17. Gas collector; 18. Vacuum pump; 19. Piston container; 20. Air compression system; 21. High-pressure pump.

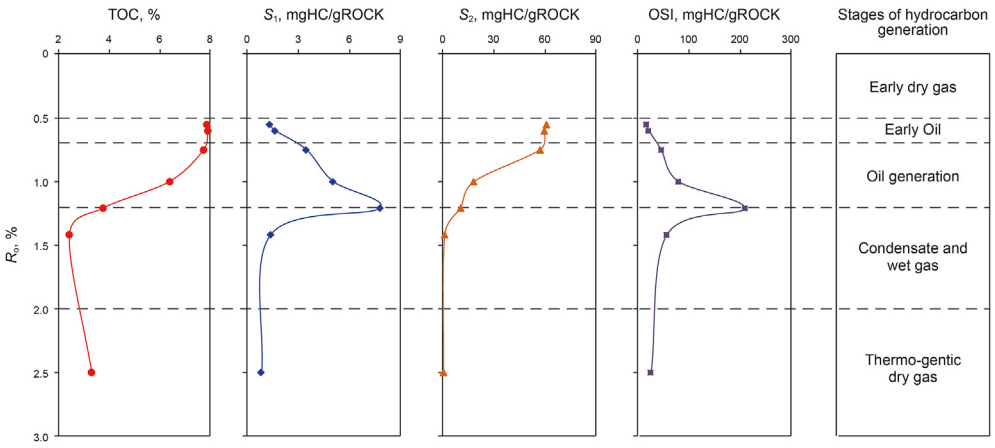

Fig. 3. Organic geochemical characteristics of the Ek_2 shale samples.

Table 2
Organic geochemical characteristics of the Ek_2 shale samples.

Sample code	R_o, %	TOC, %	S_1, mg/g	S_2, mg/g	T_{max}, °C	HI, mg/g	OSI. mg/g	EOM, %	Stages of hydrocarbon generation
OS	0.55	7.87	1.28	60.94	446	805	16.26	0.04	Early oil generation
PY-300	0.60	7.89	1.61	59.52	448	824	20.41	0.05	Early oil generation
PY-325	0.75	7.74	3.46	56.89	448	780	44.70	0.12	Oil generation
PY-350	1.00	6.39	5.04	18.36	430	266	78.87	0.39	Peak oil
PY-375	1.21	3.73	7.78	10.27	435	270	208.58	0.22	Condensate and wet gas
PY-400	1.42	2.41	1.34	1.11	–	34	55.60	0.05	Condensate and wet gas
PY-500	2.50	3.30	0.83	0.40	–	11	25.15	0.01	Dry gas

TOC decreased by a further 16.8%. When the temperature was in the range of 400–500 °C (1.42% < R_o ≤ 2.50%), the sample entered the high mature to over mature stage. The TOC of the sample slightly increased at 500 °C (Fig. 3, Table 2).

The S_1 and oil saturation index (OSI, equivalent to S_1/TOC × 100 (Jarvie, 2012b)) of the shale samples initially increased and subsequently decreased with the increasing maturity. S_1 and OSI increased continuously from the low mature to the high mature stages (T ≤ 375 °C), reaching their maximum at 375 °C. Subsequently, it gradually decreased during the high mature to over mature stages (375 °C < T ≤ 500 °C). The S_2 and HI of source rocks decreased with the increasing maturity (Table 2, Fig. 3).

4.2. Hydrocarbon products

4.2.1. Total hydrocarbons generated, retained, and expelled

The amount of total hydrocarbons generated, liquid hydrocarbons generated, expelled liquid hydrocarbons, and retained hydrocarbons initially increased and subsequently decreased as experimental temperature and pressure increased. In contrast, the amount of gas generated increased monotonically with increasing experimental temperature and pressure. In low mature stage (T ≤ 325 °C, R_o ≤ 0.75%), the amounts of hydrocarbons generated, expelled, and retained were low. In mature stage (325 °C < T ≤ 375 °C, 0.75% < R_o ≤ 1.21%), a large amount of liquid hydrocarbons was generated at 350 °C (corresponding to an R_o of 1.00%). In addition, the amounts of total hydrocarbons generated, liquid hydrocarbons generated, and retained hydrocarbons reached their peaks in this stage. Compared with the amount of natural gas released in the low mature stage, natural gas increased relatively rapidly in the mature stage, but liquid hydrocarbons still predominated over gas in this stage. At temperatures lower than 350 °C, fewer liquid hydrocarbons were expelled from the shale samples, and the majority of hydrocarbon products remained in the shale samples. The retained hydrocarbons constituted the main part of the total hydrocarbons generated.

As the temperature continued to increase, the amount of hydrocarbons expelled increased, whereas the amounts of total hydrocarbons generated, liquid hydrocarbons generated, and retained hydrocarbons began to decrease. In high mature stage (375 °C < T ≤ 400 °C, 1.21% < R_o ≤ 1.42%), the amounts of total hydrocarbons generated, liquid hydrocarbons generated, and retained hydrocarbons decreased. Furthermore, the amount of natural gas generated and liquid hydrocarbons expelled increased. The amount of expelled liquid hydrocarbons reached its maximum at 400 °C and subsequently decreased. Natural gas predominated during the over mature stage (400 °C < T ≤ 500 °C, 1.42% < R_o ≤ 2.50%), during which natural gas production increased rapidly. The amounts of total hydrocarbons, liquid hydrocarbons generated, and retained hydrocarbons decreased in this stage, and the amounts of liquid hydrocarbons generated and retained decreased considerably. Over-maturity not only caused the decomposition of kerogen and retained liquid hydrocarbons but also resulted in natural gas generation by consuming kerogen and retained hydrocarbons (Table 3).

4.2.2. Aliphatic hydrocarbon molecular composition of the retained and expelled hydrocarbons

Table 4 and Fig. 4 present the molecular composition characteristics of the retained and expelled hydrocarbons at various evolutionary stages. The *n*-alkane distribution of the expelled hydrocarbons ranged from nC_{14} to nC_{32}, and the main peak in carbon number was observed to range from nC_{17} to nC_{21}. The *n*-alkane distribution of the retained hydrocarbons ranged from nC_{14} to nC_{36}, and the main peak in carbon number was observed to range from nC_{19} to nC_{23}. During each stage of thermal evolution, the highest carbon number and the main peak carbon number of the expelled hydrocarbons were lower than those of the corresponding retained hydrocarbons (Table 4, Fig. 4). Aliphatic hydrocarbons with small molecular weights were preferentially expelled from the source rocks. The ratio of light to heavy normal alkanes ($\sum nC_{21}^{-}/\sum nC_{22}^{+}$), odd–even predominance (OEP), the ratio of pristane to nC_{17} (Pr/nC_{17}), and the ratio of phytane to nC_{18} (Ph/nC_{18}) indicate that the maturities of the retained and expelled oil changed with increasing experimental temperature (Table 4, Fig. 4).

Comparative results indicate that the molecular compositions of the aliphatic hydrocarbons in the expelled and retained hydrocarbons change regularly but differently during thermal evolution. In low mature stage (T ≤ 325 °C, R_o < 0.75%), the hydrocarbon products were mainly large-molecule components accompanied by a small quantity of small-molecule components. Small molecule components with high mobility tended to be expelled, but large-molecule hydrocarbons were mostly retained in the samples, resulting in considerably high $\sum nC_{21}^{-}/\sum nC_{22}^{+}$ values in expelled hydrocarbons and low $\sum nC_{21}^{-}/\sum nC_{22}^{+}$ values in retained hydrocarbons. In this stage, the OEP values of the expelled hydrocarbons and retained hydrocarbons were 1.29–1.15 and 1.43–1.29, respectively. Both these values were greater than 1, indicating an obvious odd-carbon preference. The Pr and Ph contents were high, and the values of Pr/nC_{17} and Ph/nC_{18} were large. All these geochemical indicators reflect the low maturity of the crude oil in this stage.

During the high mature to over mature stages (400 °C < T ≤ 500 °C, 1.42% < R_o ≤ 2.5%), the hydrocarbon products were mainly dry gas in the form of expelled hydrocarbons. The biomarkers from liquid hydrocarbons exhibited little significance as indicators of thermal maturity and hydrocarbon generation in this stage.

4.3. Pore structure characteristics

4.3.1. N_2 adsorption curves

The adsorption branches of the original and experimental samples transform gradually from type III to type II in this study, according to the latest classification standard of IUPAC (Thommes et al., 2015) (Fig. 5). Type III isotherms usually show an obvious uptake at very low P/P_0 and a steep upward trend when P/P_0 is close

Table 3
Hydrocarbon products from the pyrolysis experiments of the Ek_2 shale samples.

Sample	Expelled gas HC (mgHC/gRock)	Expelled liquid HC (mgHC/gRock)	Retained HC (mgHC/gRock)	Liquid HC generated (mgHC/gRock)	Total HC generated (mgHC/gRock)
PY-300	0.09	0.43	5.18	5.60	5.70
PY-325	0.38	1.10	12.05	13.16	13.54
PY-350	2.32	3.01	39.43	42.44	44.75
PY-375	4.12	16.51	22.17	38.68	42.80
PY-400	9.60	21.78	6.48	28.26	37.85
PY-500	21.11	6.03	0.49	6.53	27.64

Table 4
Aliphatic hydrocarbon molecular composition characteristics of the expelled and retained hydrocarbons.

	Expelled hydrocarbon						Retained hydrocarbon					
Temperature, °C	300	325	350	375	400	500	300	325	350	375	400	500
Maximum Peak	C_{17}	C_{17}	C_{21}	C_{19}	C_{17}	C_{21}	C_{23}	C_{23}	C_{23}	C_{21}	C_{20}	C_{22}
$\sum nC_{21}^{-}/\sum nC_{22}^{+}$	4.46	6.09	1.09	1.46	3.95	1.04	0.47	0.51	0.51	0.61	1.13	0.74
OEP	1.29	1.15	1.07	1.02	1.00	1.04	1.43	1.29	1.20	1.02	1.00	1.01
Pr/nC_{17}	1.05	0.92	0.43	0.13	0.06	0.17	1.10	0.95	0.27	0.11	0.04	0.08
Ph/nC_{18}	1.58	0.89	0.48	0.10	0.05	0.12	1.66	0.87	0.29	0.08	0.03	0.14

OEP (odd–even predominance): $(nC_{21} + 6 \times nC_{23} + nC_{25})/(4 \times nC_{22} + 4 \times nC_{24})$.

to 1. In contrast, type II isotherms lack a sharp knee at very low P/P_0 and retain the finite adsorbed amount at the saturation pressure ($P/P_0 = 1$). The maximum adsorption volume of each shale sample increased continuously with increasing temperature, reaching a maximum at 400 °C and then decreasing with the further temperature increase. Hysteresis loops were observed for all shale samples. The amplitude of the hysteresis loops of the N_2 adsorption and desorption curves increased with increasing temperature. The hysteresis loop was the largest at 400 °C, and the shape of the loop gradually changed from Type H_4 to Type H_3 and then to a combination of Types H_2b and H_3.

Different types of pores resulted in loops of different shapes. The formation of an H_2b hysteresis loop is related to pore blockage, usually corresponding to ink-bottle-shaped pores. The formation of an H_3 hysteresis loop corresponds to slit pores with a tapered structure, while the formation of an H_4 type hysteresis loop is caused by slit pores with a parallel plate structure (Thommes et al., 2015). At low mature stage ($T \leq 325$ °C, $R_o < 0.75\%$), the micropores in the shale primarily exhibited a parallel plate structure or a tapered structure. In mature stage (325 °C $< T \leq$ 375 °C, $0.75\% < R_o \leq 1.21\%$), the pores predominantly exhibited a tapered structure. In high mature to over mature stages (375 °C $< T$, $1.21\% < R_o \leq 2.5\%$), ink-bottle-shaped pores formed. Thus, with increasing maturity, the micropores gradually changed from a parallel plate structure or tapered structure to an ink-bottle-shaped structure (Fig. 5).

4.3.2. Mercury intrusion curves

The mercury intrusion curves indicate two-stage distributions for all samples, except for sample PY-350. In the low mature stage ($T \leq 325$ °C, $R_o < 0.75\%$), the curves of the samples rise rapidly at saturation values below 40% and then increased slowly. At 350 °C (corresponding to $R_o = 1.00\%$), the shale sample's mercury intrusion curve rises at a relatively constant rate. In the high mature to over mature stages (375 °C $< T \leq 500$ °C, $1.21\% < R_o \leq 2.50\%$), the curve rises sharply at saturation values below 10%; it subsequently rises slowly (Fig. 6). As the degree of thermal maturity increased, the mercury withdrawal efficiency initially increased and subsequently decreased. Sample PY-375 exhibits the highest mercury withdrawal efficiency (77.59%). The decrease in the mercury withdrawal efficiency of samples such as PY-375, PY-400, and PY-500 may be related to the thermal evolution that increased the number of ink-bottle-shaped pores, changing the wettability of the surface. Indeed, the presence of fine-pore-neck and ink-bottle-shaped pores made it difficult for all the mercury to be withdrawn from the porous media.

4.3.3. Pore size distribution

The pore (throat) size distribution (from 2 nm to 40 μm) in shale at various evolutionary stages was determined based on the pore size distributions of mesopores (2–50 nm) and macropores (>50 nm) at the evolutionary stages derived from the N_2 adsorption and mercury injection tests. Pores with sizes smaller than 50 nm were detected based on the results of the N_2 adsorption test, whereas pores with sizes of 50 nm–400 μm were detected based on the results of the mercury intrusion test. Thus, 50 nm was the common point between these two techniques (Fig. 7). Table 5 presents the pore structure parameters obtained from the original sample and pyrolytic samples, including the specific surface area and pore volume. The specific surface areas and pore volumes determined by the N_2 adsorption test are 1.898–8.114 m^2/g and 0.007–0.025 cm^3/g, respectively, whereas those determined via the mercury intrusion test are 6.359–19.660 m^2/g and 0.090–0.277 cm^3/g, respectively.

Except for sample PY-350, which exhibits a multipeak distribution with two main peaks at 130–300 nm and 50–90 μm, all samples exhibits a bimodal distribution. For low-maturity samples, including samples OS, PY-300, and PY-325, the pore size distribution shows a small peak at <50 nm and a large peak at approximately 50–100 nm. As maturity increases, the pore size distributions of samples PY-375, PY-400, and PY-500 shows a small peak at approximately 10–20 nm and a sharp peak at hundreds of nanometers. While the pore diameter corresponding to the peak decreased in the mesopore range. During thermal evolution, the number of pores of small diameter (dozens of nanometers) increased. As for large pores, the pore diameter corresponding to the peak position gradually increased with increasing maturity.

5. Discussion

5.1. Evolution of pore structure characteristics

The specific surface areas and pore volumes observed in the study are the results of hydrocarbon generation and expulsion, without consideration of the pores occupied by retained oil or extractible organic matter, perhaps resulting in the underestimation of the pore volume and specific surface area of the Ek_2 shale. Integrating the variation in pore structure parameters with the variation in retained oil across a range of thermal maturities would provide a clearer view of the impact of pore structure variation during thermal maturation. The specific surface areas and pore volumes of the samples increased with increasing thermal maturity (Fig. 8), whereas retained oil first increased and then decreased with increasing thermal maturity. Retained oil reached its maximum at 1.00% R_o, indicating not only that increasing thermal maturity brought about the increase in pore volume and specific surface area, but also that the occlusion of original pores or newly generated pores by the generated liquid hydrocarbon caused an underestimation of pore volume and specific area for R_o values below 1.00%. The pore volume and specific surface area of the PY-500 sample decreased slightly at R_o values above 2.00%. With the expulsion of natural gas, the exerted confining pressure may have caused the collapse of some microscopic pores, slightly decreasing the overall pore volume and specific surface area. The increases in specific surface area and pore volume with increasing temperature were considerably greater in magnitude when based on the

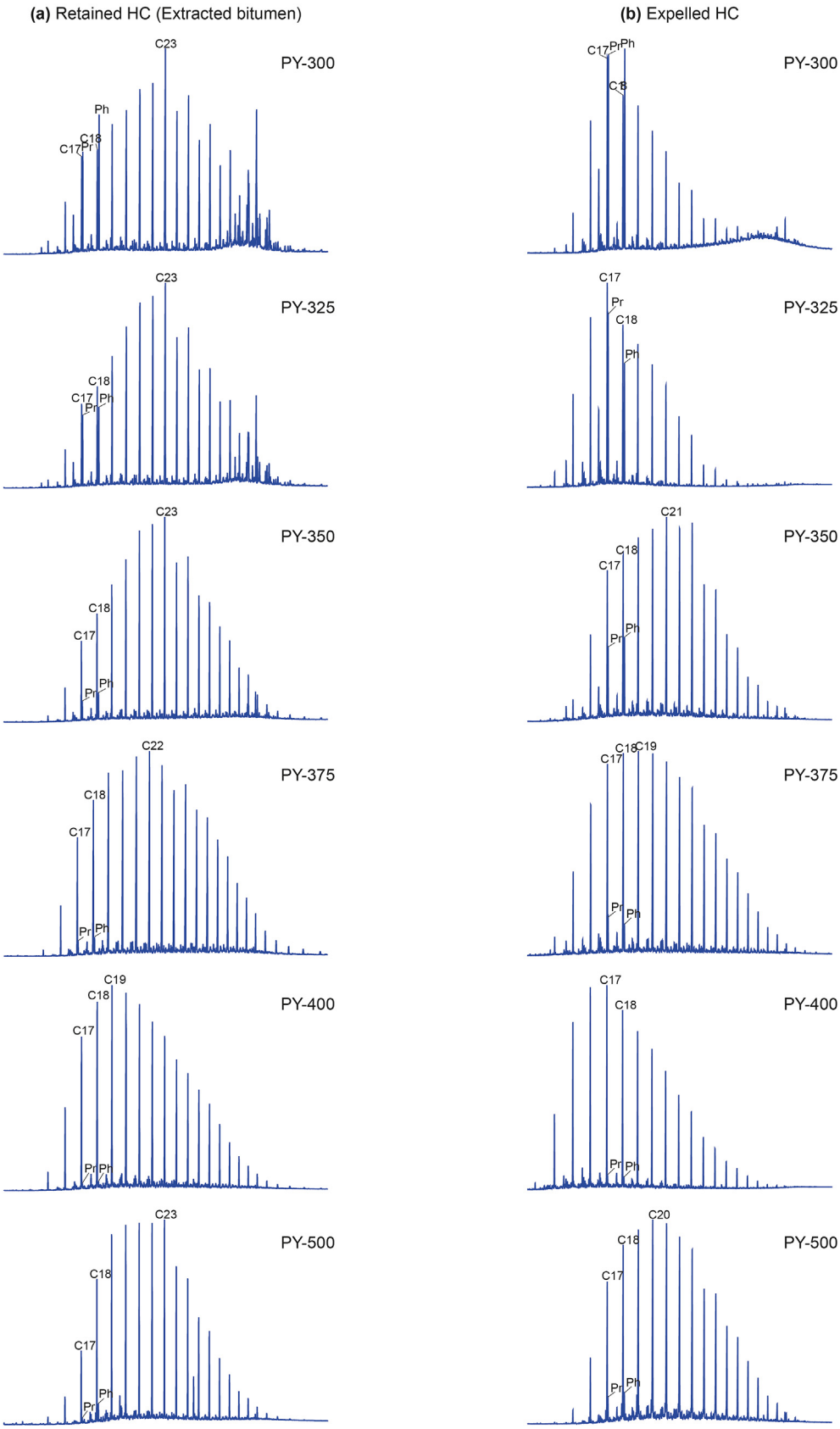

Fig. 4. *N*-alkane and isoprenoid distributions: (a) retained hydrocarbons, and (b) expelled hydrocarbons generated during the pyrolysis experiments.

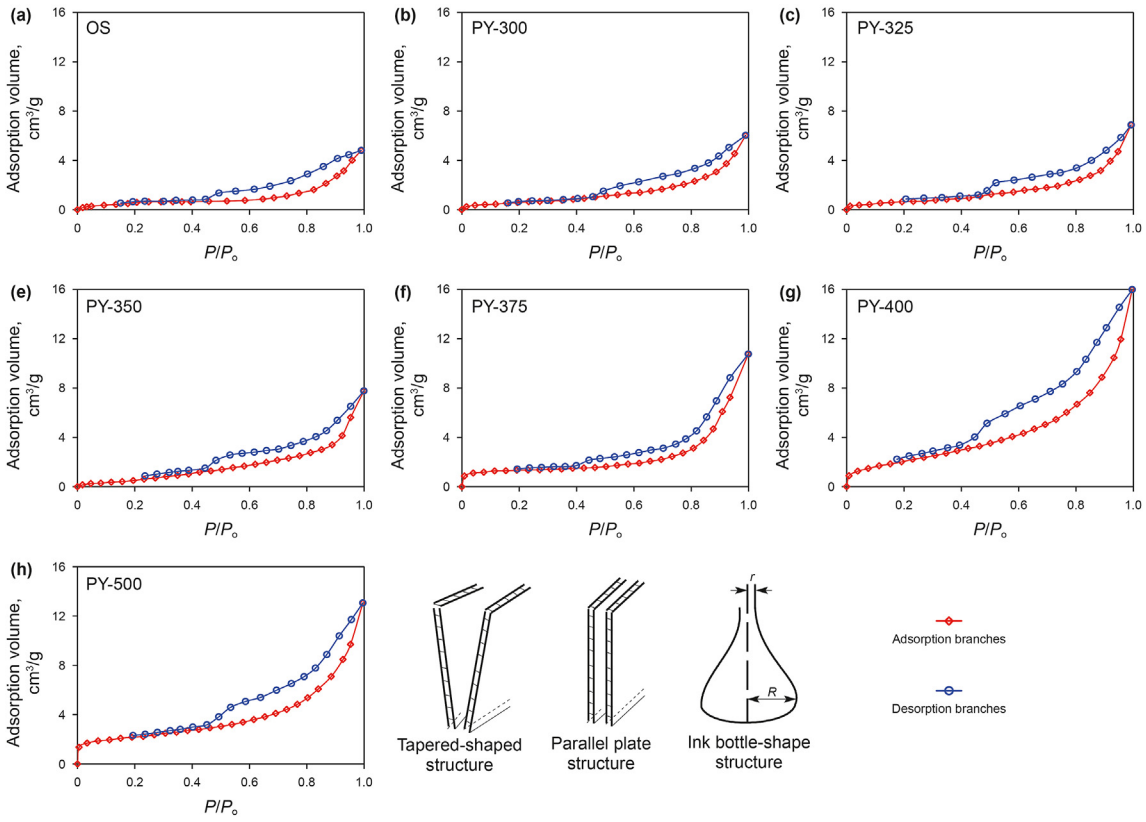

Fig. 5. N_2 adsorption curves: (a) shale samples from the original shale, and (b–h) shale samples after the pyrolysis experiments.

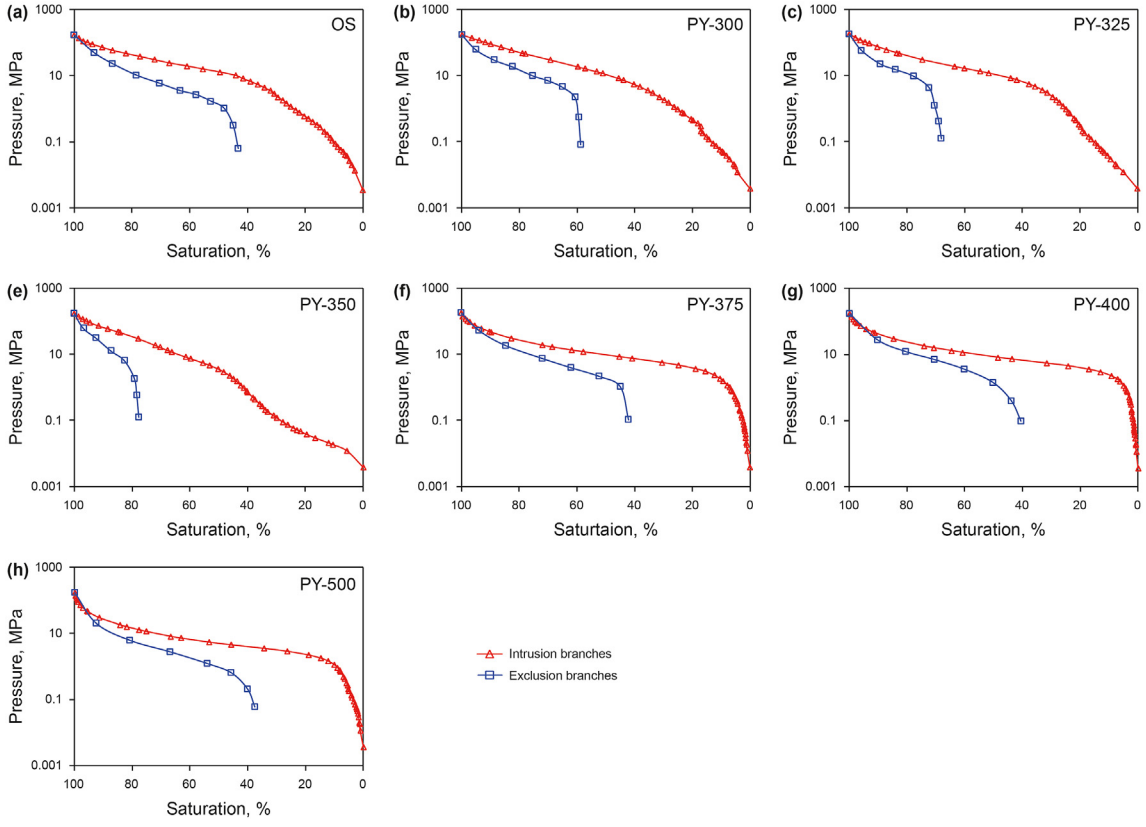

Fig. 6. Mercury intrusion curves: (a) shale samples from the original shale, and (b–h) shale samples after the pyrolysis experiments.

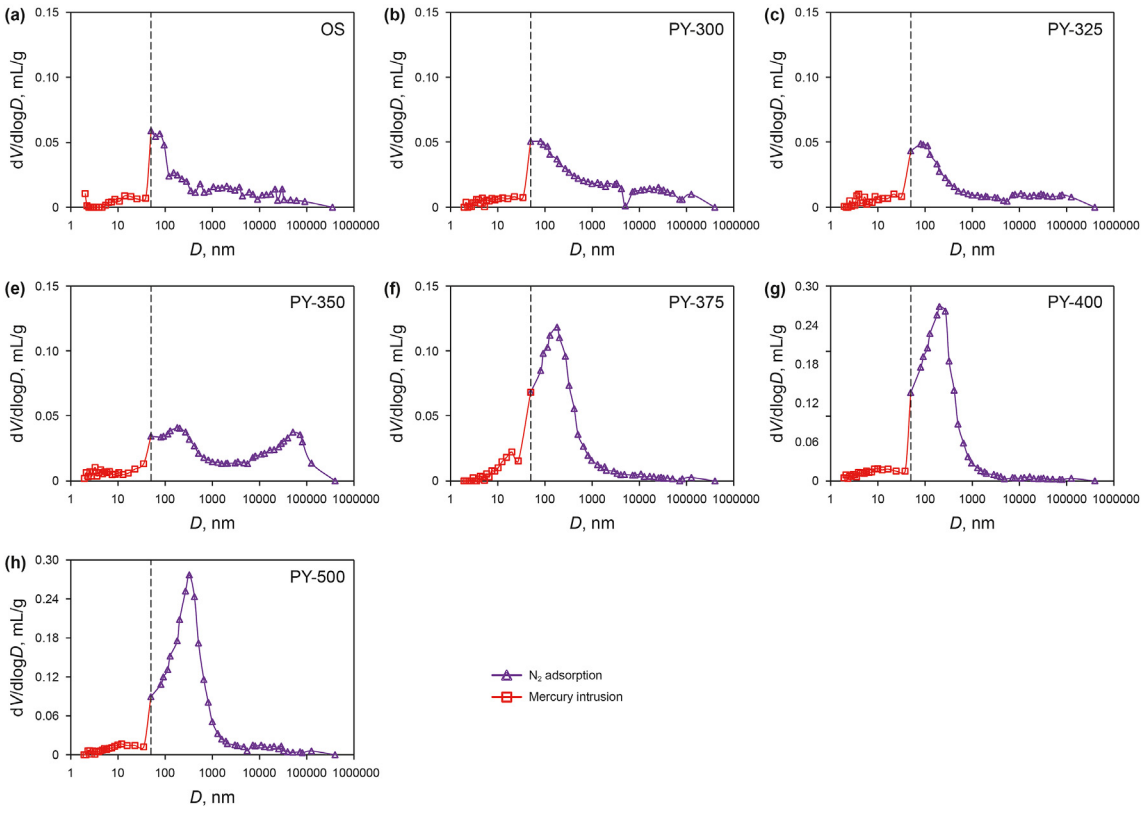

Fig. 7. Pore (throat) diameter distribution: (a) shale samples from the original shale, and (b–h) shale samples after the pyrolysis experiments. The boundary between micropores and mesopores is defined by dashed lines at a diameter of 50 nm.

Table 5
Pore structure parameters from the original shale sample (OS) and pyrolysis samples (PY).

Sample ID	N_2 adsorption		Mercury intrusion	
	Specific surface area, m^2/g	Pore volume, cm^3/g	Specific surface area, m^2/g	Pore volume, cm^3/g
OS	1.898	0.007	6.359	0.090
PY-300	1.907	0.009	7.974	0.112
PY-325	2.409	0.011	5.739	0.081
PY-350	2.874	0.012	8.587	0.121
PY-375	5.040	0.017	9.488	0.134
PY-400	8.114	0.025	19.660	0.277
PY-500	7.691	0.020	18.721	0.264

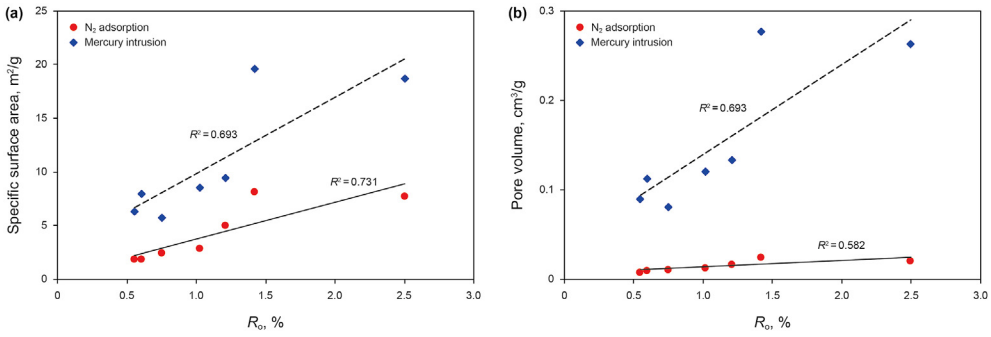

Fig. 8. Correlations between thermal maturity and pore structure parameters based on samples from the original shale as well as the shale samples after pyrolysis experiments: (a) SSA vs. R_o and (b) TPV vs. R_o.

mercury injection test than when based on the nitrogen adsorption test. This disparity was due to the wider pore-size detection range of the former, allowing it to identify more pores in the same shale sample.

The shale pore development characteristics were affected by the shale microstructure. Organic pores in shales are mostly smaller than 200 nm in diameter; however, the pores related to the mineral matrix are mostly larger (Chen et al., 2016; Katz and Arango, 2018). The characteristics of pore development with maturation varied with pore size. At R_o values below 1.00%, retained oil content underwent a clear increase. Meanwhile, increasing maturity did not considerably affect the pore-size-dependent changes in pore distribution, probably because liquid hydrocarbons were retained in the pores during the "oil-window" stage, causing pore occlusion (Wei et al., 2014). At R_o values above 1.00%, retained oil content gradually decreased to zero, with gaseous hydrocarbons beginning to predominate. Pore volumes for pore diameters of <10 nm, 10–50 nm, and 50–200 nm first increased and then decreased, but variation was slight. In contrast, pore volumes for pore diameters >200 nm increased monotonically. The expulsion of gaseous hydrocarbons exposed more pores, resulting in a higher effective pore volume. The increasing level of thermal maturity brought about new pore generation, especially for organic pores, as well as pore connectivity, as observed in the Longmaxi Shale (Huang et al., 2020). The process of organic pore formation and evolution has been previously outlined and can be divided into four periods: 1) scattered small spotted spherical pore formation, 2) gradual pore growth with incipient pore–pore contact, 3) large ellipsoidal pore formation due to interconnectivity, and 4) rapid pore expansion producing pores with "pit" structure (Huang et al., 2020).

5.2. Impact of hydrocarbon products on pore evolution

Different types of hydrocarbons were generated at different stages of thermal evolution, and the pore structure characteristics of the shale samples varied accordingly.

The pore structure characteristics of pores with different pore diameter varied with maturity. Pores of diameter >50 nm predominated in the shale pore system and were the main contributor to pore volume (Fig. 10). In the low mature stage ($T \leq 325$ °C, $R_o < 0.75\%$), TOC did not change considerably, and the amount of liquid hydrocarbons generated was small. The majority of crude oil components of high molecular weight and density were retained in the shale samples. The C_{21}^{-}/C_{22}^{+} value was small, and the pore volumes of various types of pores decreased slightly, indicating occlusion of the primary pores in the low mature stage by crude oil components of high molecular weight and density that were retained in the shale (Han et al., 2017).

In mature stage (325 °C < $T \leq$ 350 °C, 0.75% < $R_o \leq$ 1.00%), the TOC of the sample decreased considerably, and the low-molecular-weight hydrocarbon content increased. The C_{21}^{-}/C_{22}^{+} value increased, and the pore volumes of those pores (<100 nm) not occupied by liquid hydrocarbons did not change considerably. As for peak oil generation, retained oil content reached its maximum, and organic pores were mostly occluded by crude oil or bitumen. Furthermore, the volume of inorganic pores of diameter above 200 nm increased, probably because of the organic acid-generated dissolution pores in minerals such as feldspar and calcite (Yuan et al., 2013). Dissolution pores were observed in the Ek_2 shale with pore sizes ranging from several hundred nm to several μm (Fig. 9).

In the highly mature stage (375 °C < $T \leq$ 400 °C, 1.21% < $R_o \leq$ 1.42%), TOC continued to decrease as maturity increased, with retained oil content decreasing. Furthermore, the liquid hydrocarbons originally trapped in the shale decomposed into gaseous phases. The low-molecular-weight hydrocarbon content increased, and the mobility of hydrocarbon products improved considerably, resulting in a constant increase in the quantity of expelled hydrocarbons. Thus, for each pore size class, the number of pores increased continuously due to the expulsion of hydrocarbons and additional pore formation. The increase in the number of pores of diameter beyond 50 nm was particularly significant, and the total pore volume increased to its maximum at this stage.

When R_o exceeds 2.00%, the shale entered over mature stage, mainly generating gaseous hydrocarbons, and the retained oil content is close to 0. TOC increased slightly because of polycondensation reactions that occurred after the thermal degradation of kerogen. Kerogen transforms to asphalt and natural gas content significantly increases, generating nanoscale organic pores. Additionally, some minerals decomposed at high temperatures to form new inorganic pores. Nonetheless, the total pore volume of the shale decreased. Although pore volumes for pore diameters beyond 200 nm increased, pore volumes decreased for pore diameters in the ranges of <10 nm, 10–50 nm, and 50–200 nm. As the degree of maturity further increased and the sample reached the over mature stage, small pores connected to form larger pores and even pit-structure pores. However, the total pore volume decreased due to external pressure and the expulsion of gaseous hydrocarbons (Milliken and Curtis, 2016) (Fig. 10).

6. Conclusions

In this study, the pore structure evolution of lacustrine organic-rich shale was investigated via pyrolysis experiments, allowing the following conclusions to be drawn.

The generation and expulsion of hydrocarbons caused changes in pore structure during thermal evolution. Organic pores were generated by the thermal decomposition of organic matter. In addition, organic acids generated during hydrocarbon generation

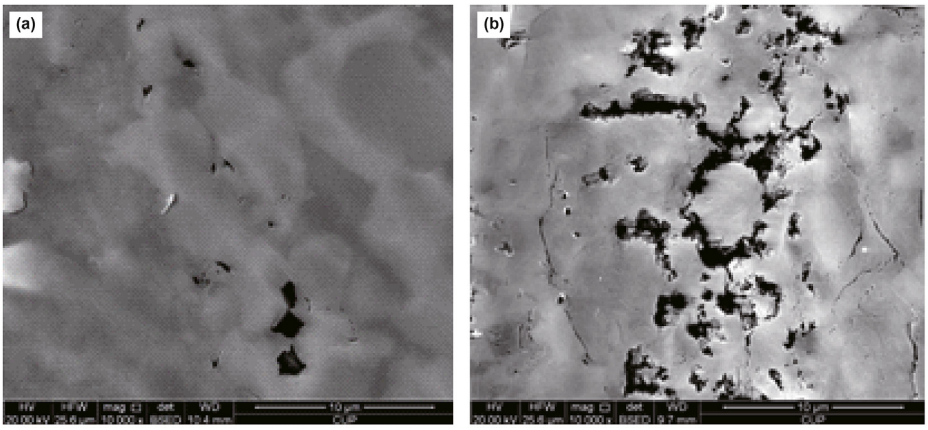

Fig. 9. Images of dissolution pores in Ek_2 shale: (a) G33 well, 2485.23 m, irregular dissolution pores in calcite, and (b) F29 well, 2447.32 m, serrated dissolution pores in feldspar.

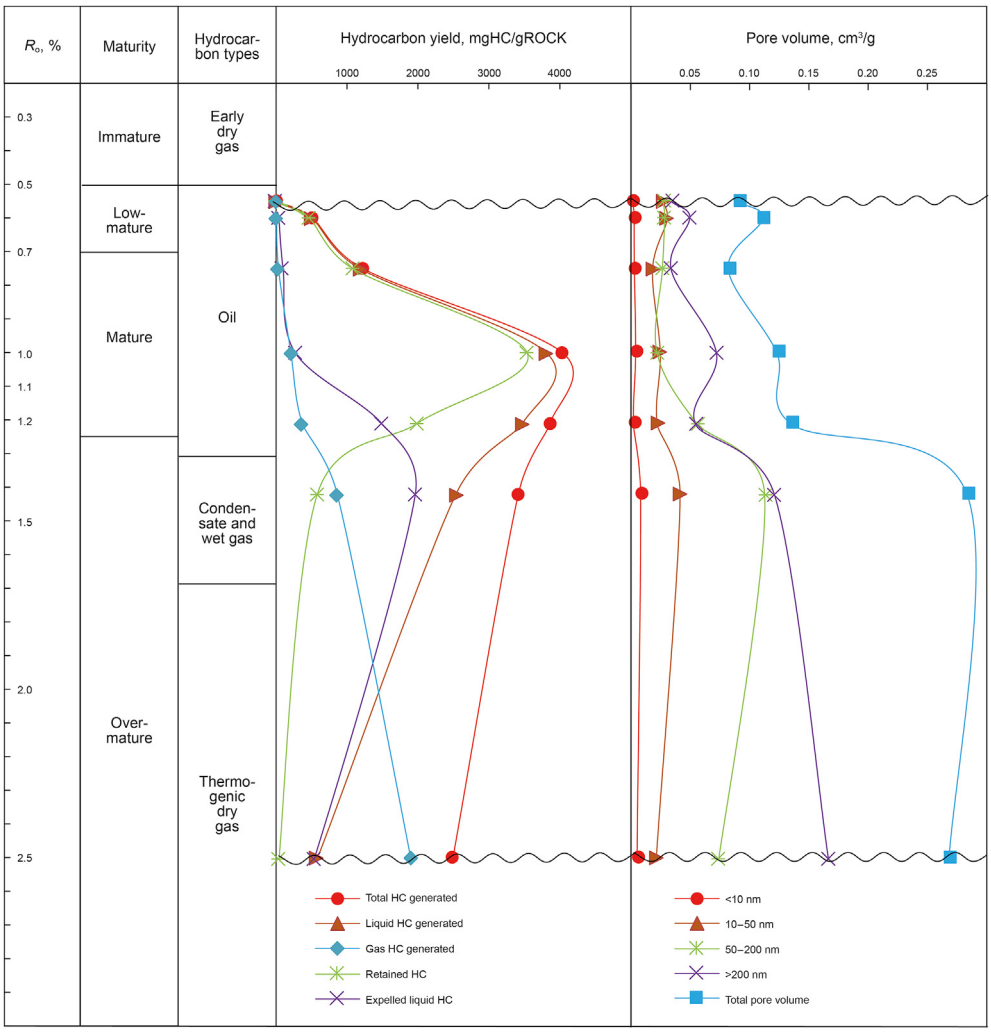

Fig. 10. Evolution of pore volume and hydrocarbon generation during thermal maturation.

caused the dissolution of minerals, such as feldspar and calcite, increasing the number, specific surface area, and volume of pores. The blockage of nanoscale pores by hydrocarbons or bitumen during thermal evolution clearly affected pore structure.

In the early oil-window stage, viscous, dense, liquid hydrocarbons or bitumen was generated by thermal degradation of kerogen and restricted the increase in pore volume for various pore types by occluding the newly formed organic pores or the original mineral-matrix pores. The viscosity and density of the liquid hydrocarbons decreased as thermal maturity increased. The liquid hydrocarbons were subsequently expelled from the shale samples; the pore volume considerably increased during this process. In the dry gas generation stage, small pores, particularly organic pores, begin to interconnect and form large pores or pit-structure pores, thus increasing the pore volume contribution of large pores. This study provides a basis for examining variation in hydrocarbon production during the thermal evolution of shale and the relationship of these variation with shale reservoir evolution.

Acknowledgments

This study was supported by the National Natural Science Foundation of China (Grant Nos. 42072150, 41372144) and the State Science and Technology Major Project of China (Grant No. 2017ZX05049001-008).

References

Alcantar-Lopez, L., 2016. Understanding organic matter structural changes with increasing thermal maturity from oil shale plays through SEM imaging. In: Unconventional Resources Technology Conference http://doi:URTeC control ID number 2456170.

Aplin, A.C., Macquaker, J.H.S., 2011. Mudstone diversity: origin and implications for source, seal, and reservoir properties in petroleum systems. AAPG Bull. 95 (12), 2031–2059. https://doi.org/10.1306/03281110162.

Athy, L.F., 1930. Density, porosity, and compaction of sedimentary rocks. AAPG Bull. 14 (1), 1–24. https://doi.org/10.1306/3d93289e-16b1-11d7-8645000102c1865d.

Camp, W., 2014. Diagenesis of organic-rich shale: views from Foraminifera Penetralia, Eagle Ford Formation, Maverick Basin, Texas. In: AAPG Rocky Mountain Section Meeting. https://doi.org/10.2118/200481-pa. Denver, Colorado.

Cardott, B.J., Landis, C.R., Curtis, M.E., 2015. Post-oil solid bitumen network in the Woodford Shale, USA-A potential primary migration pathway. Int. J. Coal Geol. 139, 106–113. https://doi.org/10.1016/j.coal.2014.08.012.

Chalmers, G.R.L., Bustin, R.M., Power, I.M., 2012. Characterization of gas shale pore systems by porosimetry, pycnometry, surface area, and field emission scanning electron microscopy/transmission electron microscopy image analyses: examples from the Barnett, Woodford, Haynesville, Marcellus, and Doig units. AAPG Bull. 96 (6), 1099–1119. https://doi.org/10.1306/10171111052.

Chalmers, G.R.L., Bustin, R.M., Powers, I., 2009. A pore by any other name would be as small: the importance of meso- and microporosity in shale gas capacity. In: AAPG Annual Convention and Exhibition. https://doi.org/10.2118/158833-ms. Denver, CO.

Chandra, D., Bakshi, T., Vishal, V., 2021. Thermal effect on pore characteristics of shale under inert and oxic environments: insights on pore evolution. Microporous Mesoporous Mater. 316, 110969. http://doi:10.1016/j.micromeso.2021.110969.

Chen, J., Xiao, X.M., 2014. Evolution of nanoporosity in organic-rich shales during thermal maturation. Fuel 129, 173–181. https://doi.org/10.1016/

j.fuel.2014.03.058, 2014.
Chen, Q., Zhang, J.C., Tang, X., et al., 2016. Relationship between pore type and pore size of marine shale: an example from the Sinian-Cambrian Formation, upper Yangtze region, South China. Int. J. Coal Geol. 158, 13–28. https://doi.org/10.1016/j.coal.2016.03.001.
Clarkson, C.R., Solano, N., Bustin, R.M., et al., 2013. Pore structure characterization of North American shale gas reservoirs using USANS/SANS, gas adsorption, and mercury intrusion. Fuel 103, 606–616. https://doi.org/10.1016/j.fuel.2012.06.119.
Curtis, M.E., Cardott, B.J., Sondergeld, C.H., et al., 2012. Development of organic porosity in the Woodford Shale with increasing thermal maturity. Int. J. Coal Geol. 103, 26–31. https://doi.org/10.2118/160158-ms.
Deng, H.C., Fu, M.Y., Zhou, W., et al., 2021. The pores evolution of lacustrine shale induced by smectite-to-illite conversion and hydrocarbon generation: upper Triassic Yanchang Formation, Ordos Basin, China. J. Petrol. Sci. Eng. 202, 108460. https://doi.org/10.1016/j.petrol. 2021.108460.
Dong, Q.Y., Liu, X.P., Zhang, P.P., et al., 2015. Assessment on hydrocarbon-generation potential of tight oil and prediction of favorable zones in Kong-2 member of the Kongnan Area. Special Oil Gas Reservoirs 22 (4), 51–56. https://doi.org/10.1002/gj.3963/v3/decision1 (in Chinese).
Goral, J., Walton, I., Andrew, M., et al., 2019. Pore system characterization of organic-rich shales using nanoscale-resolution 3D imaging. Fuel 258, 116049. https://doi.org/10.1016/j.fuel.2019. 116049.
Guan, M., Liu, X.P., Jin, Z.J., et al., 2020. The heterogeneity of pore structure in lacustrine shales: insights from multifractal analysis using N_2 adsorption and mercury intrusion. Mar. Petrol. Geol. 114, 104150. https://doi.org/10.1016/j.marpetgeo.2019.104150.
Guo, H.J., Jia, W.L., He, R.L., et al., 2020. Distinct evolution trends of nanometer-scale pores displayed by the pyrolysis of organic matter-rich lacustrine shales: implications for the pore development mechanisms. Mar. Petrol. Geol. 121, 104622. http://doi:10.1016/j.marpetgeo. 2020.104622.
Han, Y.H., Horsfield, B., Wirth, R., et al., 2017. Oil retention and porosity evolution in organic-rich shales. AAPG Bull. 101 (6), 807–827. https://doi.org/10.1306/09221616069.
Huang, C., Ju, Y.W., Zhu, H.J., 2020. Investigation of formation and evolution of organic matter pores in marine shale by helium ion microscope: an example from the Lower Silurian Longmaxi Shale, South China. Mar. Petrol. Geol. 120, 104550. http://doi: 10.1016/j.marpetgeo.2020. 104550.
Hunt, J.M., 1996. Petroleum Geochemistry and Geology. San Francisco.
Hutton, A.C., 1987. Petrographic classification of oil shales. Int. J. Coal Geol. 8 (3), 203–231. https://doi.org/10.1016/0166-5162(87)90032-2.
Ilgen, A.G., Heath, J.E., Akkutlu, I.Y., et al., 2017. Shales at all scales: exploring coupled processes in mudrocks. Earth Sci. Rev. 166, 132–152 https://doi.org/j.earscirev.2016.12.013.
İnan, S., Al Badairy, H., İnan, T., et al., 2018. Formation and occurrence of organic matter-hosted porosity in shales. Int. J. Coal Geol. 199, 39–51. https://doi.org/10.1016/j.coal. 2018.09.021.
Jarvie, D.M., 2012a. Shale resource systems for oil and gas: Part 1-shale-gas resource systems. In: Breyer, A. (Ed.), Shale Reservoir-Giant Resources for the 21st Century, 97. AAPG Memoir, pp. 69–87. https://doi.org/10.1002/9781119039228.ch3.
Jarvie, D.M., 2012b. Shale resource systems for oil and gas: Part 2-shale-oil resource systems. In: Breyer, A. (Ed.), Shale Reservoir-Giant Resources for the 21st Century, 97. AAPG Memoir, pp. 89–119. https://doi.org/10.3390/books978-3-03928-876-2.
Jennings, D.S., Antia, J., 2013. Petrographic characterization of the Eagle Ford Shale, south Texas: mineralogy, common constituents, and distribution of nanometer scale nanometer scale pore types, Electron Microscopy of Shale Hydrocarbon Reservoirs. AAPG Memoir 102, 101–113. https://doi.org/10.1306/13391708m1023586.
Katz, B.J., Arango, I., 2018. Organic porosity: a geochemist's view of the current state of understanding. Org. Geochem. 123, 1–16. https://doi.org/10.1002/9780470777930.ch3.
Ko, L.T., Loucks, R.G., Milliken, K.L., et al., 2017. Controls on pore types and pore-size distribution in the Upper Triassic Yanchang Formation, Ordos Basin, China-Implications for pore-evolution models of lacustrine mudrocks. Interpretation 5 (2), 127–148. https://doi.org/10.1190/int-2016-0115.1.
Ko, L.T., Loucks, R.G., Zhang, T.W., et al., 2016. Pore and pore network evolution of Upper Cretaceous Boquillas (Eagle Ford–equivalent) mudrocks: results from gold tube pyrolysis experiments. AAPG Bull. 100 (11), 1693–1722. https://doi.org/10.1306/04151615092.
Kuchinskiy, V., 2013. Organic porosity study: porosity development within organic matter of the Lower Silurian and Ordovician source rocks in Poland shale gas trend. In: American Association of Petroleum Geologists Annual Convention and Exhibition. https://doi.org/10.3390/min10020108. Pittsburgh, PA.
Kuila, U., Prasad, M., 2013. Specific surface area and pore-size distribution in clays and shales. Geophys. Prospect. 61 (2), 341–362. https://doi.org/10.1111/1365-2478.12028.
Lai, J., Wang, G.W., Wang, Z., et al., 2018. A review on pore structure characterization in tight sandstones. Earth Sci. Rev. 177, 436–457. https://doi.org/10.1130/abs/2018am-321368.
Land, L.S., Milliken, K.L., McBride, E.F., 1987. Diagenetic evolution of cenozoic sandstones, Gulf of Mexico sedimentrary Basin. Sediment. Geol. 50, 195–225. https://doi.org/10.1016/0037-0738 (87)90033-9.
Lazar, O.R., Bohacs, K.M., Macquaker, J.H.S., et al., 2015. Capturing key attributes of fine-grained sedimentary rocks in outcrops, cores, and thin sections: momenclature and description guidelines. J. Sediment. Res. 85 (3), 230–246. https://doi.org/10.2110/jsr.2015.11.
Li, J., Zhao, J.Z., Wei, X.S., et al., 2019. Origin of abnormal pressure in the upper Paleozoic shale of the Ordos Basin, China. Mar. Petrol. Geol. 110, 162–177. http://doi:10.1016/j.marpetgeo.2019. 07.016.
Liu, D., Li, Z., Jiang, Z., et al., 2019. Impact of laminae on pore structures of lacustrine shales in the southern Songliao Basin, NE China. J. Asian Earth Sci. 182, 103935. https://doi.org/10.1016/j.jseaes.2019.103935.
Liu, X.P., Lai, J., Fan, X.C., et al., 2020. Insights in the pore structure, fluid mobility and oiliness in oil shales of Paleogene Funing Formation in Subei Basin, China. Mar. Petrol. Geol. 114, 104228. https://doi.org/10.1016/j.marpetgeo.2020.104228.
Löhr, S.C., Baruch, E.T., Hall, P.A., et al., 2015. Is organic pore development in gas shales influenced by the primary porosity and structure of thermally immature organic matter? Org. Geochem. 87, 119–132. https://doi.org/10.1016/j.orggeochem.2015.07.010.
Loucks, R.G., Reed, R.M., Ruppel, S.C., et al., 2009. Morphology, genesis, and distribution of nanometer-scale pores in siliceous mudstones of the Mississippian Barnett shale. J. Sediment. Res. 79 (12), 848–861. https://doi.org/10.2110/jsr.2009.092.
Loucks, R.G., Reed, R.M., Ruppel, S.C., et al., 2012. Spectrum of pore types and networks in mudrocks and a descriptive classification for matrix-related mudrock pores. AAPG Bull. 96 (6), 1071–1098. https://doi.org/10.1306/08171111061.
Loucks, R.G., Reed, R.M., 2014. Scanning-electron-microscope petrographic evidence for distinguishing organic matter pores associated with depositional organic matter versus migrated organic matter in mudrocks. Gulf Coast Assoc. Geol. Sociaties Transac. 3, 51–60. https://doi.org/10.1130/abs/2020am-352717.
Mastalerz, M., Schimmelmann, A., Drobniak, A., et al., 2013. Porosity of Devonian and Mississippian New Albany Shale across a maturation gradient: insights from organic petrology, gas adsorption, and mercury intrusion. AAPG Bull. 97 (10), 1621–1643. https://doi.org/10.1306/04011312194.
McBride, E.F., 1989. Quartz cement in sandstones: a review. Earth Sci. Rev. 26 (1-3), 69–112. https://doi.org/10.1016/0012-8252(89)90019-6.
Merriman, R.J., Highley, D.E., Cameron, D.G., 2003. Definition and characteristics of very-fine grained sedimentary rocks clay, mudstone, shale and slate. British Geol. Survey. 1–16. https://doi.org/10.1130/0091-7613(1978)6<745:lcovfg>2.0.co;2.
Milliken, K.L., 2014. A compositional classification for grain assemblages in fine-grained sediments and sedimentary rocks. J. Sediment. Res. 84 (12), 1185–1199. https://doi.org/10.2110/jsr.2015. 100.
Milliken, K.L., Curtis, M.E., 2016. Imaging pores in sedimentary rocks: foundation of porosity prediction. Mar. Petrol. Geol. 73, 590–608. https://doi.org/10.1016/j.marpetgeo.2016.03.020.
Milliken, K.L., Reed, R.M., McCarty, D.K., et al., 2019. Grain assemblages and diagenesis in the Vaca Muerta Formation (Jurassic-Cretaceous), Neuquén Basin, Argentina. Sediment. Geol. 380, 45–64. https://doi.org/10.1016/j.sedgeo.2018.11.007.
Milliken, K.L., Rudnicki, M., Awwiller, D.N., et al., 2013. Organic matter-hosted pore system, Marcellus Formation (Devonian), Pennsylvania. AAPG Bull. 97 (2), 177–200. https://doi.org/10.1306/07231212048.
Modica, C.J., Lapierre, S.G., 2012. Estimation of kerogen porosity in source rocks as a function of thermal transformation: example from the Mowry Shale in the Powder River Basin of Wyoming. AAPG Bull. 96 (1), 87–108. https://doi.org/10.1306/04111110201.
Nie, H.K., Li, D.H., Liu, G.X., et al., 2020. An overview of the geology and production of the Fuling shale gas field, Sichuan Basin, China. Energy Geosci. 1 (3-4), 147–164. https://doi.org/10.1016/j.engeos.2020.06.005.
Ougier-Simonin, A., Renard, F., Boehm, C., et al., 2016. Microfracturing and microporosity in shales. Earth Sci. Rev. 162, 198–226. https://doi.org/10.1016/j.earsc.2016.09.006.
Reed, R.M., Loucks, R.L., 2015. Low-thermal-maturity (<0.7% VR) mudrock pore systems: Mississippian Barnett Shale, southern fort worth Basin. Gulf Coast Assoc. Geol. Societies 4, 15–28.
Reed, R.M., Loucks, R.L., Milliken, K.L., 2012. Heterogeneity of shape and microscale spatial distribution in organic-matter-hosted pores of gas shales. In: American Association of Petroleum Geologists Annual Convention and Exhibition, Long Beach, CA. https://doi.org/10.3389/fmicb.2018.01583. Long Beach, CA.
Schlömer, S., Krooss, B.M., 1997. Experimental characterization of the hydrocarbon sealing efficiency of cap rocks. Mar. Petrol. Geol. 14 (5), 565–580. https://doi.org/10.1016/s0264-8(97)00022-6.
Seewald, J.S., 2003. Organic-inorganic interactions in petroleum-producing sedimentary basins. Nature 426 (6964), 327–333. http://doi: 10.1038/nature02132.
Selley, R.C., 1978. Porosity gradients in North Sea oil-bearing sandstones. J Geol Soc London 135 (1), 119–132. https://doi.org/10.1144/gsjgs.135.1.0119.
Slatt, R.M., O'Brien, N.R., 2011. Pore types in the Barnett and Woodford gas shales: contribution to understanding gas storage and migration pathways in fine-grained rocks. AAPG Bull. 95 (12), 2017–2030. https://doi.org/10.1306/03301110145.
Solarin, S.A., Gil-Alana, L.A., Lafuente, C., 2020. An investigation of long range reliance on shale oil and shale gas production in the U.S. market. Energy 195, 116933. https://doi/j.energy.2020.11693.
Spigolon, A.L.D., Lewan, M.D., de Barros Penteado, H.L., et al., 2015. Evaluation of the petroleum composition and quality with increasing thermal maturity as simulated by hydrous pyrolysis: a case study using a Brazilian source rock with Type I kerogen. Org. Geochem. 83-84, 27–53. https://doi.org/10.1016/

j.orggeochem.2015.03.001.
Sun, Y., Zhao, Y., Yuan, L., 2018. Quantifying nano-pore heterogeneity and anisotropy in gas shale by synchrotron radiation nano-CT. Microporous Mesoporous Mater. 258, 8–16. https://doi.org/10.1016/j.micromeso.2017.08.049.
Tang, X., Zhang, J.C., Jiang, Z.J., et al., 2015a. Characteristics of solid residue, expelled and retained hydrocarbons of lacustrine marlstone based on semi-closed system hydrous pyrolysis: implications for tight oil exploration. Fuel 162, 186–193. https://doi.org/10.1016/j.fuel. 2015. 09. 009.
Tang, X., Zhang, J.C., Jin, Z.J., et al., 2015b. Experimental investigation of thermal maturation on shale reservoir properties from hydrous pyrolysis of Chang 7 shale, Ordos Basin. Mar. Petrol. Geol. 64, 165–172. https://doi.org/10.1016/j.marpetgeo.2015.02.046.
Teillet, T., Fournier, F., Gisquet, F., et al., 2019. Diagenetic history and porosity evolution of an Early Miocene carbonate buildup (Upper Burman Limestone), Yadana gas field, offshore Myanmar. Mar. Petrol. Geol. 109, 589–606. https://doi.org/10.1016/j.marpetgeo.2019.06.044.
Thommes, M., Kaneko, K., Neimark, A.V., et al., 2015. Physisorption of gases, with special reference to the evaluation of surface area and pore size distribution (IUPAC Technical Report). Pure Appl. Chem. 87 (9-10), 1051–1069. https://doi.org/10.1515/ci-2016-0119.
Wang, P.F., Zhang, C., Li, X., et al., 2020. Organic matter pores structure and evolution in shales based on the he ion microscopy (HIM): a case study from the Triassic Yanchang, Lower Silurian Longmaxi and Lower Cambrian Niutitang shales in China. J. Nat. Gas Sci. Eng. 84, 103682. https://10.1016/j.jngse.2020.103682.
Wei, L., Mastalerz, M., Schimmelmann, A., et al., 2014. Influence of Soxhlet-extractable bitumen and oil on porosity in thermally maturing organic-rich shales. Int. J. Coal Geol. 132, 38–50. https://doi.org/10.1016/j.coal.2014.08.003, 2014.
Wei, M., Zhang, L., Xiong, Y., et al., 2016. Nanopore structure characterization for organic-rich shale using the non-local-density functional theory by a combination of N_2 and CO_2 adsorption. Microporous Mesoporous Mater. 227, 88–94 https://doi.org/j.micromeso.2016.02.050.
Wirth, R., 2009. Focused ion beam (FIB) combined with SEM and TEM: advanced analytical tools for studies of chemical composition, microstructure and crystal structure in geomaterials on a nanometre scale. Chem. Geol. 261 (3), 217–229. https://doi.org/10.1016/j.chemgeo. 2008.05.019.
Wu, S.T., Yang, Z., Zhai, X., et al., 2019. An experimental study of organic matter, minerals and porosity evolution in shales within high-temperature and high-pressure constraints. Mar. Petrol. Geol. 102, 377–390 https://doi.org/10.16/j.marpetgeo.2018.12.014.
Xu, H., Tang, D., Zhao, J., et al., 2015. A precise measurement method for shale porosity with low-field nuclear magnetic resonance: a case study of the Carboniferous–Permian strata in the Linxing area, eastern Ordos Basin, China. Fuel 143, 47–54 https://doi.org/j.fuel.2014.11.034.
Yang, Y., Aplin, A.C., 2010. A permeability–porosity relationship for mudstones. Mar. Petrol. Geol. 27 (8), 1692–1697. https://doi.org/10.1016/j.marpetgeo.2009.07.001.
Yang, Z., Zou, C.N., Wu, S.T., et al., 2019. Formation, distribution and resource potential of the "sweet areas (sections)" of continental shale oil in China. Mar. Petrol. Geol. 102, 48–60. https://doi.org/10.1016/j.marpetgeo.2018.11.049.
Yuan, G.H., Cao, Y.C., Yang, T., et al., 2013. Porosity enhancement potential through mineral dissolution by organic acids in the diagenetic process of clastic reservoir. Earth Sci. Front. 20 (5), 207–219. https://doi.org/10.1021/acs.energyfuels.9b00486 (in Chinese).
Zargari, S., Canter, K.L., Prasad, M., 2015. Porosity evolution in oil-prone source rocks. Fuel 153, 110–117. https://doi.org/10.1190/segam2014-0950.1.
Zhao, X.Z., Pu, X.G., Zhou, L.H., et al., 2020. Typical geological characteristics and exploration practices of lacustrine shale oil: a case study of the Kong-2 member strata of the Cangdong Sag in the Bohai Bay Basin. Mar. Petrol. Geol. 113, 103999. https://doi.org/10.1016/j.marpetgeo.2019.08.027.
Zhao, X.Z., Zhou, L.H., Pu, X.G., et al., 2018b. Geological characteristics of shale rock system and shale oil exploration in a lacustrine basin: a case study from the Paleogene 1st sub-member of Kong 2 Member in Cangdong sag, Bohai Bay Basin, China. Petrol Explor. Exploit. 45 (3), 361–372. https://doi.org/10.1016/s1874(18)30043-0.
Zhao, X.Z., Zhou, L.H., Pu, X.G., et al., 2018a. The sedimentary structure and petroleum geologic significance of the ring belt of the closed lake basin: an integrated interpretation of well and seismic data of the Kong2 Member in Cangdong Sag, Central Bohai Bay Basin. China. Interpretation. 6 (2), 283–298. https://doi.org/10.1190/int-2017-0041.1.
Zhao, X.Z., Zhou, L.H., Pu, X.G., et al., 2019. Exploration breakthroughs and geological characteristics of continental shale oil: a case study of the Kongdian Formation in the Cangdong Sag, China. Mar. Petrol. Geol. 102, 544–556. https://doi.org/10.1016/j.marpetgeo.2018.12.020.
Zou, C.N., Zhu, R.K., Chen, Z., et al., 2019. Organic-matter-rich shales of China. Earth Sci. Rev. 189, 51–78. https://doi.org/10.1021/acs.energyfuels.6b03144.s001.